



HAL
open science

Orbital selective switching of ferromagnetism in an oxide quasi two-dimensional electron gas

R. Di Capua, M. Verma, M. Radovic, V. Strocov, C. Piamonteze, E. Guedes, N. Plumb, Yu Chen, M. D'antuono, G. de Luca, et al.

► To cite this version:

R. Di Capua, M. Verma, M. Radovic, V. Strocov, C. Piamonteze, et al.. Orbital selective switching of ferromagnetism in an oxide quasi two-dimensional electron gas. *Npj Quantum Materials*, 2022, 7 (1), pp.41. 10.1038/s41535-022-00448-4 . hal-03884373v2

HAL Id: hal-03884373

<https://cnrs.hal.science/hal-03884373v2>

Submitted on 7 Dec 2022

HAL is a multi-disciplinary open access archive for the deposit and dissemination of scientific research documents, whether they are published or not. The documents may come from teaching and research institutions in France or abroad, or from public or private research centers.

L'archive ouverte pluridisciplinaire **HAL**, est destinée au dépôt et à la diffusion de documents scientifiques de niveau recherche, publiés ou non, émanant des établissements d'enseignement et de recherche français ou étrangers, des laboratoires publics ou privés.



Distributed under a Creative Commons Attribution 4.0 International License

ARTICLE OPEN



Orbital selective switching of ferromagnetism in an oxide quasi two-dimensional electron gas

R. Di Capua^{1,2}, M. Verma³, M. Radovic⁴, V. N. Strocov⁴, C. Piamonteze⁴, E. B. Guedes⁴, N. C. Plumb⁴, Yu Chen², M. D'Antuono^{1,2}, G. M. De Luca^{1,2}, E. Di Gennaro^{1,2}, D. Stornaiuolo^{1,2}, D. Preziosi⁵, B. Jouault⁶, F. Miletto Granozio², A. Sambri², R. Pentcheva³, G. Ghiringhelli^{7,8} and M. Salluzzo²✉

Multi-orbital physics in quasi-two-dimensional electron gases (q2DEGs) triggers intriguing phenomena not observed in bulk materials, such as unconventional superconductivity and magnetism. Here, we investigate the mechanism of orbital selective switching of the spin-polarization in the oxide q2DEG formed at the (001) interface between the LaAlO₃, EuTiO₃ and SrTiO₃ band insulators. By using density functional theory calculations, transport, magnetic and x-ray spectroscopy measurements, we find that the filling of titanium-bands with 3d_{xz}/3d_{yz} orbital character in the EuTiO₃ layer and at the interface with SrTiO₃ induces an antiferromagnetic to ferromagnetic switching of the exchange interaction between Eu-4f⁷ magnetic moments. The results explain the observation of the carrier density-dependent ferromagnetic correlations and anomalous Hall effect in this q2DEG, and demonstrate how combined theoretical and experimental approaches can lead to a deeper understanding of emerging electronic phases and serve as a guide for the materials design of advanced electronic applications.

npj Quantum Materials (2022)7:41; <https://doi.org/10.1038/s41535-022-00448-4>

INTRODUCTION

Since the discovery of a quasi-two-dimensional electron gas (q2DEG) at the interface between the LaAlO₃ (LAO) and SrTiO₃ (STO) band insulators¹, studies on oxide surfaces and interfaces uncovered an intriguing and rich physics, boosting the expectations for all-oxide electronics. The LAO/STO q2DEG shows remarkable properties, including electric field effect induced insulator-to-metal transition at room temperature², gate-tunable Rashba-like spin-orbit coupling^{3,4}, superconductivity^{5–7}, and magnetism⁸. From these studies, a fundamental role of the multi-orbital nature of the carriers in the electronic properties of the oxide q2DEGs clearly emerged.

The possibility to induce ferromagnetic (FM) correlations at the interface between non-magnetic oxides, combined with the large spin to charge conversion efficiency of oxide q2DEGs⁹, paves the way to applications in spintronics.

Recently, it has been shown that a feasible method to induce a spin-polarization in oxide q2DEGs is the introduction of a thin magnetic layer between LAO and STO, like EuTiO₃ (ETO) (Fig. 1a)^{10,11} and LaMnO₃¹². FM correlations were reported also in heterostructures where LAO is replaced by a ferro(ferri)-magnetic insulator, as in GdTlO₃/STO^{13,14}, EuO/STO¹⁵ and LaAl_{1–x}Mn_xO₃/STO¹⁶.

In LAO/ETO/STO, FM correlations are believed to be induced by the ordering of localized Eu²⁺ 4f⁷ magnetic moments and their coupling with Ti-3d states forming the conduction band of the q2DEG. However, the microscopic mechanism leading to these phenomena is not straightforward, as rare earth magnetic ions have usually a small hybridization with transition metal 3d orbitals. Unlike the LAO/STO q2DEG^{1–9}, there is no detailed study of the

electronic band structure of LAO/ETO/STO heterostructures, and it remains unclear whether a spin-polarized q2DEG is present in both ETO and interfacial STO layers, which is relevant for the intriguing phase diagram showing a transition from a FM to a superconducting state¹¹. Additionally, FM correlations were observed only above the Lifshitz transition, where carriers with 3d_{xz}/3d_{yz} orbital character start to contribute to the transport¹¹.

In this work, all these questions are settled by combining extensive experimental and theoretical investigations. Firstly, we show that low-temperature electrical transport, x-ray magnetic circular dichroism (XMCD) and superconducting quantum interference device (SQUID) experiments give evidence of a tunable ferromagnetism originating from the correlation between Ti- and Eu- magnetic moments. Secondly, we provide a direct picture of the q2DEG band structure by using resonant soft-x-ray photoemission spectroscopy (RESPE). These experimental observations are finally compared and blended with density functional theory calculations with on-site Hubbard terms (DFT + *U*). The latter show that the q2DEG forms at the LAO/ETO interface and extends few unit cells into the STO. FM correlations are induced by the delicate balance between different antiferromagnetic (AFM) and FM contributions to the exchange interaction between Eu-4f⁷ magnetic moments and Ti-3d electrons at the ETO/STO interface, which involves also the first STO layers, in agreement with the experiments. Moreover, the theoretical calculations show that the ferromagnetism in the q2DEG and the filling of 3d_{xz}/3d_{yz} bands take place simultaneously, explaining the electric field-induced anomalous Hall effect above the Lifshitz point¹¹, and the orbital selective switching of the spin-polarization in an oxide q2DEG.

¹Dipartimento di Fisica “E. Pancini”, Università di Napoli “Federico II”, Complesso Monte Sant’Angelo via Cinthia, I-80126 Napoli, Italy. ²CNR-SPIN, Complesso Monte Sant’Angelo via Cinthia, I-80126 Napoli, Italy. ³Department of Physics and Center for Nanointegration, University Duisburg-Essen Lotharstr. 1, D-47057 Duisburg, Germany. ⁴Photon Science Division, Paul Scherrer Institut, CH-5232 Villigen PSI, Switzerland. ⁵Université de Strasbourg, CNRS, IPCMS UMR 7504, 67034 Strasbourg, France. ⁶Laboratoire Charles Coulomb, UMR 5221, CNRS, Université de Montpellier, F-34095 Montpellier, France. ⁷Dipartimento di Fisica Politecnico di Milano, Piazza Leonardo da Vinci 32, I-20133 Milano, Italy. ⁸CNR-SPIN, Politecnico di Milano, Piazza Leonardo da Vinci 32, I-20133 Milano, Italy. ✉email: marco.salluzzo@spin.cnr.it

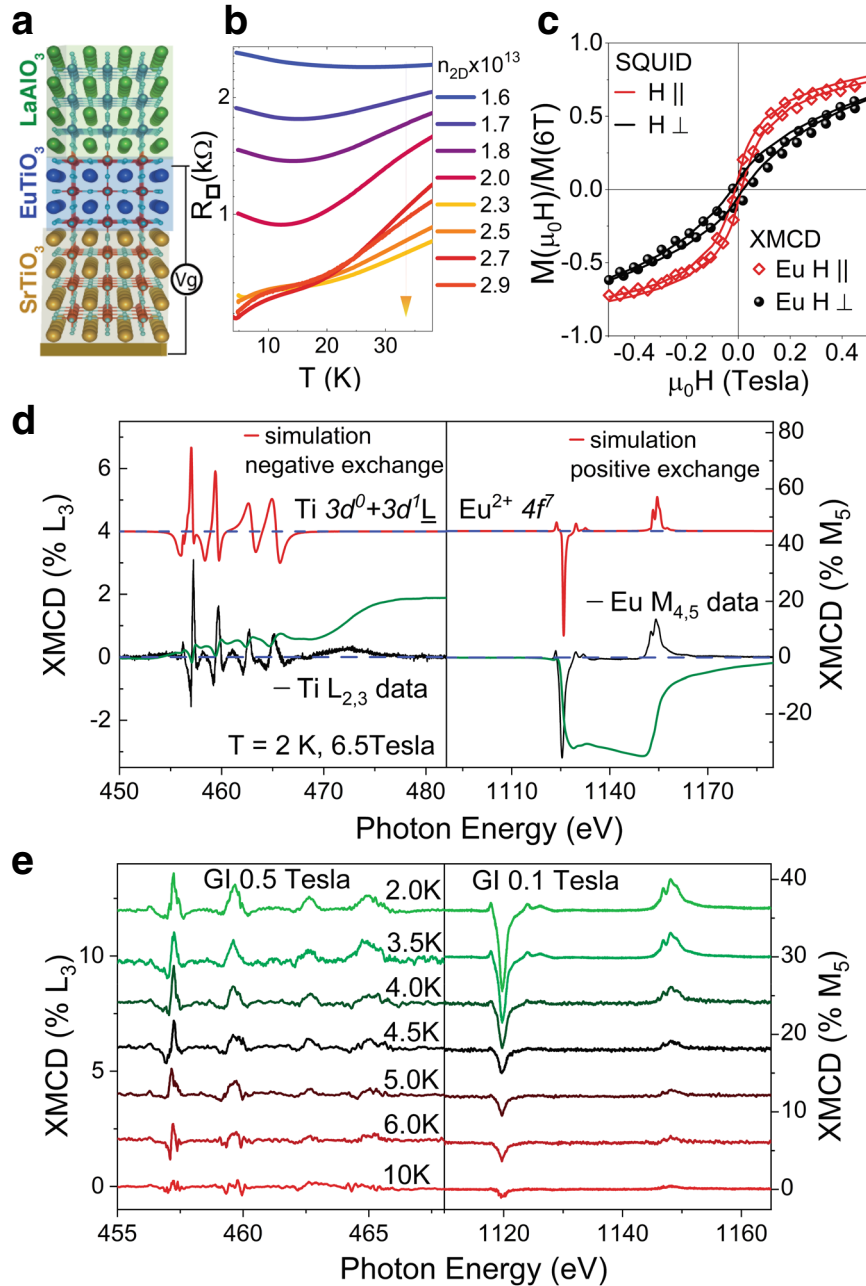


Fig. 1 Transport and magnetic properties of LAO/ETO/STO heterostructures. **a** Sketch of the LAO/ETO/STO heterostructure. In this work, the carrier concentration was tuned using electric field effect in back-gate configuration, as sketched in the figure. **b** Sheet resistance vs. temperature as a function of the gate voltage V_g . The arrow indicates increasing values of V_g from -30 to 30 V and 2D carrier density. **c** Eu-XMCD (scatter data) and SQUID magnetization (continuous lines) as function of the magnetic field parallel (red) and perpendicular (black) to the interface. The data are normalized to the saturation value. The Eu-XMCD in parallel direction is obtained by combing data acquired in grazing (60 degrees from the surface normal) and normal incidence conditions. **d** XMCD data at the Ti-L (left) and Eu-M (right) edges at 6.5 Tesla and 2 K. Red-lines are atomic multiplet simulations, green lines are integrals of the XMCD spectra (see main text). **e** Temperature dependence of the Ti-L_{2,3} (0.5 Tesla) and Eu-M_{4,5} (0.1 Tesla) edges XMCD spectra in grazing incidence conditions. Data are vertically shifted for clarity.

RESULTS

Experimental evidences of intrinsic ferromagnetic correlations

Bulk ETO is an AFM insulator with a T_N of 5.5 K, however doping or lattice strain favor a FM order in epitaxial films^{17–21}. It has a quasi-perfect structural matching with STO and a similar conduction band formed by the overlap of t_{2g} Ti-3d orbitals. By embedding few unit cells (uc) of ETO between LAO and STO using epitaxial growth by pulsed laser deposition (PLD), we realize a q2DEG characterized by electrical transport properties similar to the LAO/

STO system. However, at low temperatures and at a carrier density $>2.10^{13}$ cm⁻² tuned by electric field effect (Fig. 1a), the sheet resistance exhibits a downturn below $T=6-8$ K (Fig. 1b), which correlates with the FM transition of doped ETO¹¹. The heterostructure itself is characterized by a FM transition ($T_c = 6-8$ K) and a FM ground state, as shown in Fig. 1c, where we compare the maximum intensity of the Eu-XMCD signal (at M_5 -edge, scatter data), acquired at the X-Treme beamline of the Swiss Light Source (SLS)²², to macroscopic SQUID magnetometry data (full lines) at

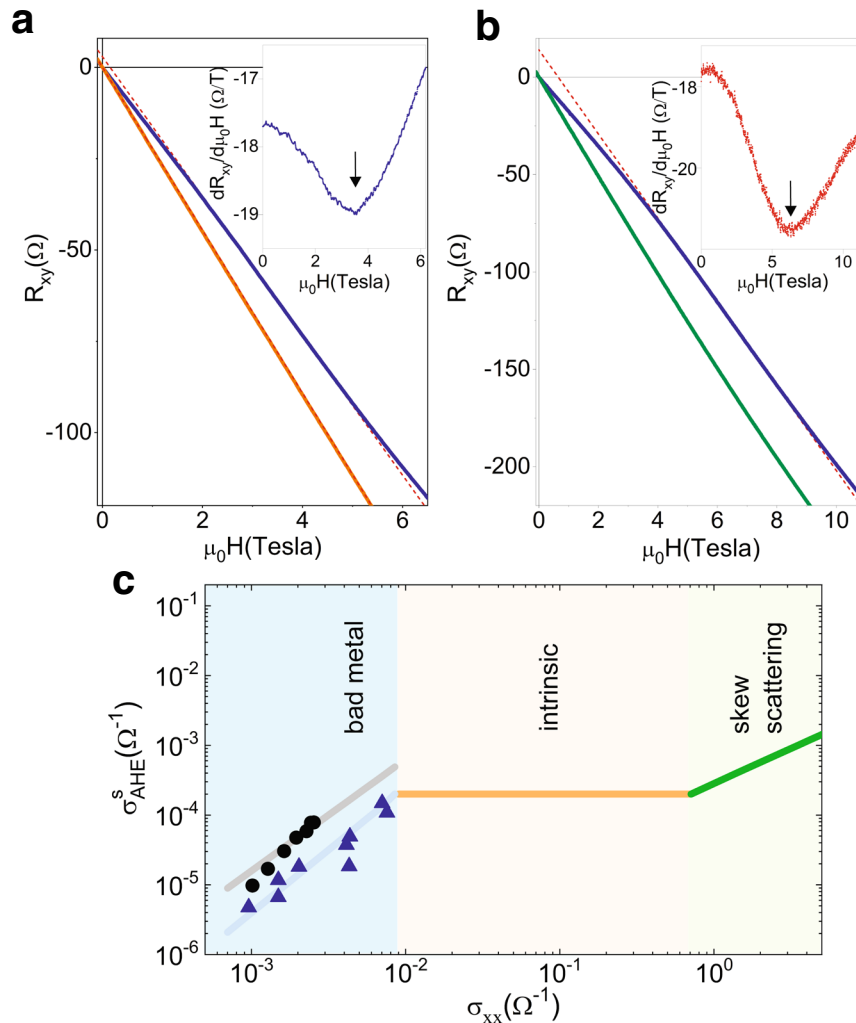


Fig. 2 Analysis of the anomalous Hall effect. Transverse (Hall) resistance R_{xy} as a function of the magnetic field of: (a) sample A at two gate voltages ($V_g = +60$ V (blue line), $V_g = -25$ V (orange line)) and 2 K; (b) sample B at $V_g = +30$ V (2 K (blue line) and 20 K (green line)). Corresponding 2 K $dR_{xy}/d\mu_0 H$ data are shown in the insets of each figure, with the arrow indicating the minimum. The minimum of the $dR_{xy}/d\mu_0 H$ is the slope of the red dashed lines fitting the data in the intermediate 3–4 Tesla range. The intercepts of these lines are the AHE components at saturation. c Anomalous Hall conductivity vs. longitudinal 2D conductivity (see main text Eq. (1)). Black dots and blue triangles refer to the two LAO/ETO/STO samples. Full lines refer to the exponent α in the relation $\sigma_{AHE} \propto (\sigma_{xx})^\alpha$: $\alpha = 1.8$ (light blue, and gray, intrinsic AHE suppressed by disorder), $\alpha = 0$ (orange, intrinsic AHE), $\alpha = 1$ (green, skew scattering).

2 K temperature as a function of the magnetic field in parallel (red) and perpendicular (black) directions. The two sets of data, normalized to the saturation value for direct comparison, show a small, although clear, hysteresis around zero magnetic field and a preferential orientation of the magnetization parallel to the interface, confirming a remanent zero-field magnetization and FM correlations. The magnetization saturates above 2–4 Tesla (depending on the sample and on the magnetic field direction) and a spin moment of the order of $4 \mu_B/\text{Eu}$ can be estimated from the XMCD using the sum-rules, indicating that Eu^{2+} -ions order ferromagnetically above these values.

To further elucidate the magnetic properties of the system, in Fig. 1d we show XAS and XMCD spectra at the Ti- $L_{2,3}$ and Eu- $M_{4,5}$ edges at 2 K and 6.5 Tesla and in Fig. 1e the XMCD temperature dependence in grazing incidence conditions (60 degrees from the surface normal). The data show that Eu- and Ti- XMCD spectra follow each other, thus are correlated. In particular the Ti- (orbital and spin) and the Eu- magnetic moments have the same temperature dependence, with a T_c of the order of 6–8 K and the same magnetic field dependence as shown in ref. 11.

In Fig. 1d, the XMCD spectra are compared to atomic multiplet simulations (red lines) for Eu^{2+} and Ti^{4+} ions in C_4 symmetry. In the calculations for the Ti-3d XMCD we used the crystal field splitting reproducing the x-ray linear dichroism data, and included a charge transfer (CT) term to account for the hybridization between Ti-3d and O-2p states in the TiO_6 cluster, i.e., a $3d^0 + 3d^1 \underline{L}$ configuration, where \underline{L} indicates a hole in the O-2p band (see Supplementary Note 1, Supplementary Fig. 1 and ref. 23). The calculations reproduce most of the features shown by the experiment. However, while a positive exchange is needed to simulate the Eu^{2+} magnetization, parallel to the magnetic field, only a negative one correctly reproduces the Ti-XMCD peaks at L_3 and L_2 . On the other hand, we also find a finite and positive Ti-XMCD integral that, according to the sum rules²⁴, corresponds to a sizeable Ti-3d orbital moment, m_{orb} , of the order of $-0.05 \mu_B/\text{Ti}$. Following the Hund's rules, the sign of the orbital moment corresponds to an opposite, finite, Ti-spin moment, m_{spin} , parallel to the Eu-spin moment. The order of magnitude of m_{spin} is $0.07 \mu_B/\text{Ti}$, thus the total Ti-magnetic moment is of the order of $0.02\text{--}0.03 \mu_B/\text{Ti}$. However, this value has to be considered only an estimate for the order of magnitude of the moment, since the spin

sum rules are heavily affected from the mixing of the L_3 and L_2 edges and inadequate for a precise quantification²⁴.

However, the Ti-XMCD integral and the Ti- magnetic moment are expected to be null for a Ti^{4+} state, even in the presence of a CT between Ti-3d and neighbor O-2p states. Thus, the only way to explain the results is the presence of two contributions to the spectra: (i) a $3d^0 + 3d^1L$ contribution, with a negative exchange interaction between the ligand Ti-3d electrons and the Eu^{2+} magnetic moments, which gives rise to the observed sign of the XMCD; (ii) a second contribution coming from Ti- $3d^1$ electronic states, with their associated magnetic moments, parallel to the magnetic field and to the Eu^{2+} spin-moments, which explain the non-zero integral of the XMCD. These results suggest different typologies of exchange interactions between Eu and Ti ions, i.e., an AFM one between Eu^{2+} and Ti- $3d^0 + 3d^1L$ states, and a FM exchange between the Eu^{2+} and Ti- $3d^1$ spin-moments.

The FM correlations in the q2DEG, and the magnetic field dependence of the magnetization, reveals in the Hall effect data¹¹. In Fig. 2a, b we show data on two representative samples, sample A (Fig. 2a, $V_g = -25$ V and $V_g = +60$ V at 2 K), and sample B (Fig. 2b, $V_g = +30$ at 2 K and at 20 K, well-above the FM Tc). A linear Hall effect is present for low gate voltage (curve at $V_g = -25$ V in Fig. 2a), indicating single band transport. For positive gate voltages and low temperature, instead, both samples exhibit a non-linear Hall effect. The 2 K non-linear Hall effect is characterized by a high field (>5–6 Tesla) curvature change due to the two-band transport above the Lifshitz point ($n_{2D} = 1.9 \cdot 10^{13} \text{ cm}^{-2}$), associated to the contribution of both light ($3d_{xy}$) and heavy ($3d_{xz}/3d_{yz}$) bands, and a low field (<2–4 Tesla) curvature change due to the anomalous Hall effect (AHE). Following the method used in refs. 11,18, the 2D anomalous resistivity at saturation, ρ_{AHE} is the intercept to zero field of a line fitting the data in the intermediate field region (red dashed lines in Fig. 2a, b). This region can be precisely identified as the field-range at which the $dR_{xy}/d\mu_0H$ (insets of Fig. 2a, b) reaches a minimum, and the slope of the fitting line is the corresponding value of $dR_{xy}/d\mu_0H$ (more details about the fitting procedure are shown in Supplementary Note 2 and Supplementary Figs. 3 and 4). Above the FM Tc, the AHE vanishes, and the Hall effect data can be nicely reproduced by a simple two-band model (Fig. 2b).

Further insights on the nature of the AHE is obtained by comparing the 2D anomalous conductivity, σ_{AHE} , to the longitudinal one, σ_{xx} estimated according to Eqs. (1) and (2):

$$\sigma_{xx} = \frac{\rho_{xx}^{2D}(0)}{(\rho_{AHE})^2 + (\rho_{xx}^{2D}(0))^2} \quad (1)$$

$$\sigma_{AHE} = \frac{\rho_{AHE}}{(\rho_{AHE})^2 + (\rho_{xx}^{2D}(0))^2} \quad (2)$$

where $\rho_{xx}^{2D}(0)$ is the zero field 2D longitudinal resistivity. The origin of the AHE can be attributed to different mechanisms, which can be phenomenologically distinguished using the relation between σ_{AHE} and σ_{xx} . According to the literature²⁵, most of the materials showing an AHE can be classified in the following three regimes: (i) a high conductivity range, where $\sigma_{AHE} \propto \sigma_{xx}$ and the observed AHE is attributed to scattering from unwanted magnetic impurities (skew scattering); (ii) an intermediate conductivity range, where σ_{AHE} is independent from σ_{xx} and the AHE is related only to the Berry curvature of the involved bands (intrinsic AHE); (iii) a bad metal range where $\sigma_{AHE} \propto (\sigma_{xx})^\alpha$, with α in the interval 1.6–1.8, where the intrinsic AHE is suppressed by the disorder. In the latter two ranges the AHE is due to the spin-polarization of the carriers and to the spin-orbit coupling breaking time and inversion symmetry. Data collected on LAO/ETO/STO samples, with carrier densities tuned by a back-gate voltage, are shown in Fig. 2c. We found a correlation $\sigma_{AHE} \propto (\sigma_{xx})^\alpha$, with $\alpha = 1.8$, which excludes a skew scattering mechanism and a purely intrinsic AHE. We

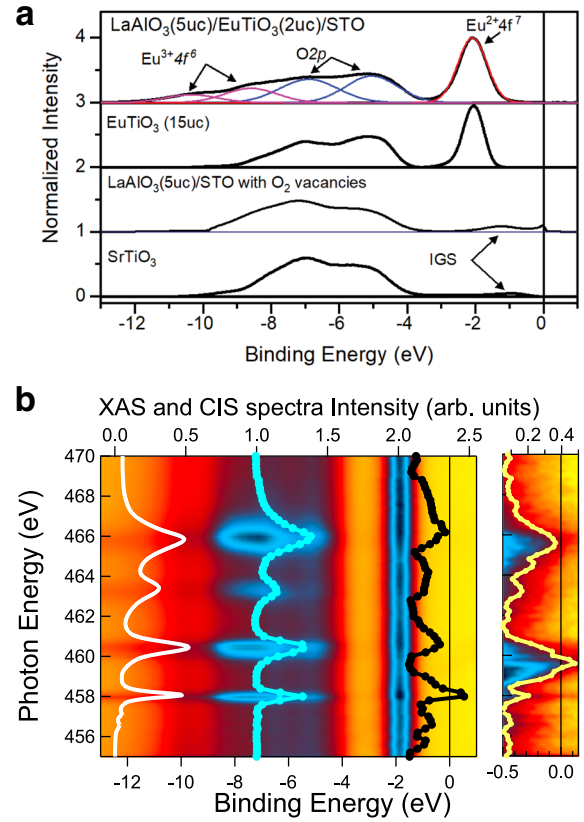


Fig. 3 RESPEs and ARPES VB data. **a** Angle integrated ARPES VB data of $SrTiO_3$, and $EuTiO_3$ q2DEG surface state, compared to angle and photon-energy integrated RESPEs VB of (001) LAO(5uc)/STO (containing oxygen vacancies) and LAO(5uc)/ETO(2uc)/STO heterostructures. Multiple gaussian fit of the LAO/ETO/STO VB profile is used to determine the Eu^{3+}/Eu^{2+} ratio. The IGS in gap states is observed only in STO and LAO/STO q2DEGs due to the presence of oxygen vacancies. **b** (left panel) RESPEs color-map of the valence band region and CIS spectra obtained integrating the RESPEs data around $BE = -2$ eV (Eu^{2+} , black scatter data) and between -7 and -4 eV (O-2p, cyan scatter data). The white line is the total electron yield XAS spectrum; (right panel) the same RESPEs map in the Fermi level region and corresponding CIS spectrum (yellow scatter data).

conclude that in LAO/ETO/STO an intrinsic AHE suppressed by disorder is at play, analogously to what found in La-doped ETO films¹⁹.

Experimental investigation of the band structure via RESPEs

In order to characterize the electronic structure of the LAO/ETO/STO system, we used the RESPEs technique at the soft-x-ray end station of the ADvanced REsonant Spectroscopies (ADRESS, X03MA) beamline of the Swiss Light Source (SLS)^{26,27}. The experimental data were acquired at base temperature (12 K) thus above the FM transition of the system.

In Fig. 3a we report angle and photon-energy integrated (across the Ti- $L_{2,3}$ edge) RESPEs VB data on (001) LAO(5uc)/ETO(2uc)/STO and on a reference PLD grown (001) LAO(5uc)/STO sample containing oxygen vacancies, i.e., cooled down from the high deposition temperature (750 °C) in a reduced oxygen pressure of the order of 10^{-5} mbar, without any high- O_2 pressure annealing process. For comparison we show also data acquired by high resolution ARPES at the SIS (Surface Interface Spectroscopy) beamline of SLS ($h\nu = 85$ eV), on reference VB of an STO crystal and of an ETO film hosting q2DEGs²⁸. Since the escape depth of the photoelectrons in the 450–470 eV range is of the order of 2 nm, in LAO(5)/ETO(2)/STO the data have contributions from both

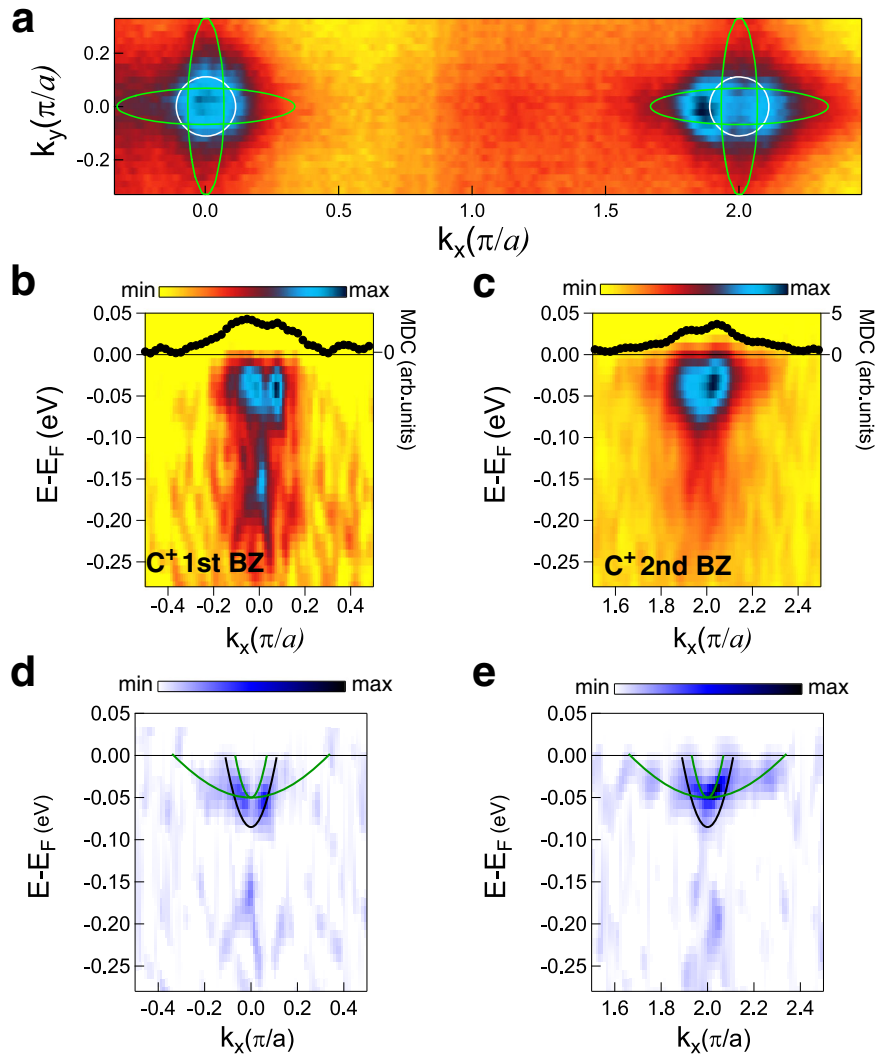


Fig. 4 Resonant angle-resolved photoemission spectra. **a** Average between circular plus and circular minus Fermi surface map of the (001) LAO/ETO/STO heterostructure. Dashed lines are Fermi surface contours of light (white) and heavy (green) bands. **b, c** E vs. k_x band dispersion maps acquired with C+ polarization in the 1st and 2nd BZ. Black scatter data on top of each band dispersion map are the Fermi level MDCs curves (integrated around E_F in a 10 meV range). All the data are measured in resonance conditions (465.5 eV). **d, e** two-dimensional curvature maps of the C+ dispersions in **b** and **c**, with tight-binding fitting of the bands (green lines $3d_{xz}$ and $3d_{yz}$ bands, black line $3d_{xy}$ band).

the ETO layers and from the interfacial STO unit cells. As a result, the VB spectra of ETO heterostructures show prominent differences with the STO and LAO/STO VB. The main one is the presence, in ETO and in LAO/ETO/STO, of a peak at -1.95 eV binding energy (BE), due to $\text{Eu}^{2+} - 4f^7$ states. Another difference, is the absence in ETO q2DEGs of the -1.0 eV in-gap state (IGS), instead observed in STO and oxygen-deficient LAO/STO²⁷. Finally, in LAO/ETO/STO we observe the evidence of a further broad feature at BE lower than -8 eV, which reflects the contribution of Eu in Eu^{3+} oxidation state: through a Gaussian deconvolution of the observed spectral features (reported in Fig. 3a), we estimated a fraction of Eu^{3+} of about 25%. This result is in agreement with atomically resolved high-resolution transmission electron microscopy and electron energy loss spectroscopy¹¹, which shows that a similar fraction of Eu^{3+} is present in the system, mostly located into the LAO layer at the interface with the ETO film. The presence of non-magnetic Eu^{3+} also explains the reduced value of the saturation magnetization per Eu ions estimated from the XMCD data ($4 \mu_B/\text{Eu}$ against $7 \mu_B/\text{Eu}$).

In Fig. 3b we report angle integrated VB-RESPES data of LAO (5uc)/ETO(2uc)/STO at photon energies $h\nu$ across the Ti-2p absorption edge resonance. The data are overlapped to TEY XAS (white line), and to Constant Initial State (CIS) spectra obtained by integrating the valence band over different binding energy ranges. CIS spectra allows the identification of the resonance of different VB features with the XAS intensity spectra. We can see that the same XAS resonances characteristic of Ti^{4+} ions appear as higher intensity signal in the RESPES map inside the contribution from the O-2p band. Similar results have been reported for the LAO/STO q2DEG²⁷, and are a consequence of the hybridization between O-2p and Ti-3d states. On the other hand, the CIS spectrum around the Fermi level, related to the q2DEG conduction band, has a different shape, reminiscent of the characteristic absorption from Ti^{3+} ions in an octahedral environment, similar to bulk LaTiO_3 ²⁹ (see Supplementary Fig. 2). Surprisingly, also the peak at -2 eV resonates with the Ti-absorption spectrum, a result which would point to a hybridization of Eu-4f with O-2p and Ti-3d states. This is rather unexpected, since 4f rare earth orbitals have usually little overlap with neighbor ions in a crystal.

In order to characterize the band structure of the LAO/ETO/STO q2DEG, in Fig. 4a we show k_x - k_y in-plane cut of the Fermi Surface (FS), obtained by averaging circular minus (C-) and circular plus (C+) polarization spectra at an incoming photon energy of 465.5 eV, resonant with the $\text{Ti}^{3+} L_2$ absorption peak. Overlapped to the map we also show Fermi surface contours associated to non-interacting electronic bands originated from atomic $\text{Ti-3d-}t_{2g}$ states: namely, a ring-shaped feature and two ellipsoidal structures oriented lengthwise along the k_x and k_y directions. The ring-shaped Fermi contour corresponds to light effective mass electrons having mainly $3d_{xy}$ orbital character, while the ellipsoidal ones are related to heavy effective masses electrons with mainly $3d_{xz}/3d_{yz}$ orbital characters. The qualitative features of the measured FS in (001) LAO/ETO/STO resemble those observed on different oxide systems characterized by the presence of a q2DEG, like the (001) STO surface^{30,31}, the (001) LAO/STO interface³²⁻³⁴, and the recently investigated (001) ETO surface²⁸. However, the FS, in particular at the 2nd Brillouin zone (BZ) where heavy bands contributions are better resolved due to matrix element effects, has a shape which departs from the simple tight-binding model of three non-interacting t_{2g} bands.

In Fig. 4b, c we show band dispersion cuts at the 1st and 2nd BZ through the Γ -point along the k_x direction (corresponding to Γ -X in

reciprocal space) with C+ polarization of the incoming photons (C+ pol, $h\nu = 465.5$ eV). Momentum Dispersion Cuts (MDCs) at the Fermi level are shown on the top of each panel. In Fig. 4d, e we show the corresponding 2D-curvature maps to highlight the different bands³⁵. Other data acquired with different polarizations of the incoming photons are shown in Supplementary Fig. 5.

The dispersive profile of the different bands were obtained by combining the 2D-curvature maps and the fit of the maxima of MDCs at several energies below the Fermi level, in analogy with previous studies on LAO/STO q2DEGs^{33,34} (see Supplementary Note 3). From simple tight-binding fitting assuming three independent bands (superimposed to the 2D curvature maps of Fig. 4d, e), we estimated the effective masses m^* at the Fermi level of each band (see Table 1). We obtained $m^* = 0.4 m_e$ for the $3d_{xy}$ band, while for the heavy bands we estimated $m^* = 0.25 m_e$ and $\sim 10 m_e$ in the “light” and “heavy” directions, respectively (m_e being the free electron mass). The $3d_{xy}$ band effective mass and the $3d_{xz}/3d_{yz}$ bands effective masses along the “light” directions are typically smaller than the ones estimated for the LAO/STO system³³. The splitting between the heavy- and light- band bottoms is of the order of ~ 35 meV at the Γ -point, considerably smaller than that usually reported for the STO-surface 2DEGs³⁰, but consistent with our recent report about the differences between the ETO and STO surface states²⁸, and in quantitative agreement with x-ray linear dichroism data on (001) LAO/ETO/STO¹¹.

Bands	k_F (\AA^{-1})	$E(0)$ (meV)	m^*/m_e
$3d_{xy}$	0.09 ± 0.01	-85 ± 5	0.4 ± 0.1
$3d_{yz}$	0.27 ± 0.02	-50 ± 5	10 ± 2
$3d_{xz}$	0.055 ± 0.005	-50 ± 5	0.25 ± 0.05

DFT + U calculations

In order to understand the mechanism at the base of the formation of the q2DEG in LAO/ETO/STO and of the spin-polarization of its carriers, we performed DFT + U calculations³⁶⁻⁴² on a non-defective $c(2 \times 2)$ LAO/ETO/STO(001) heterostructure composed of

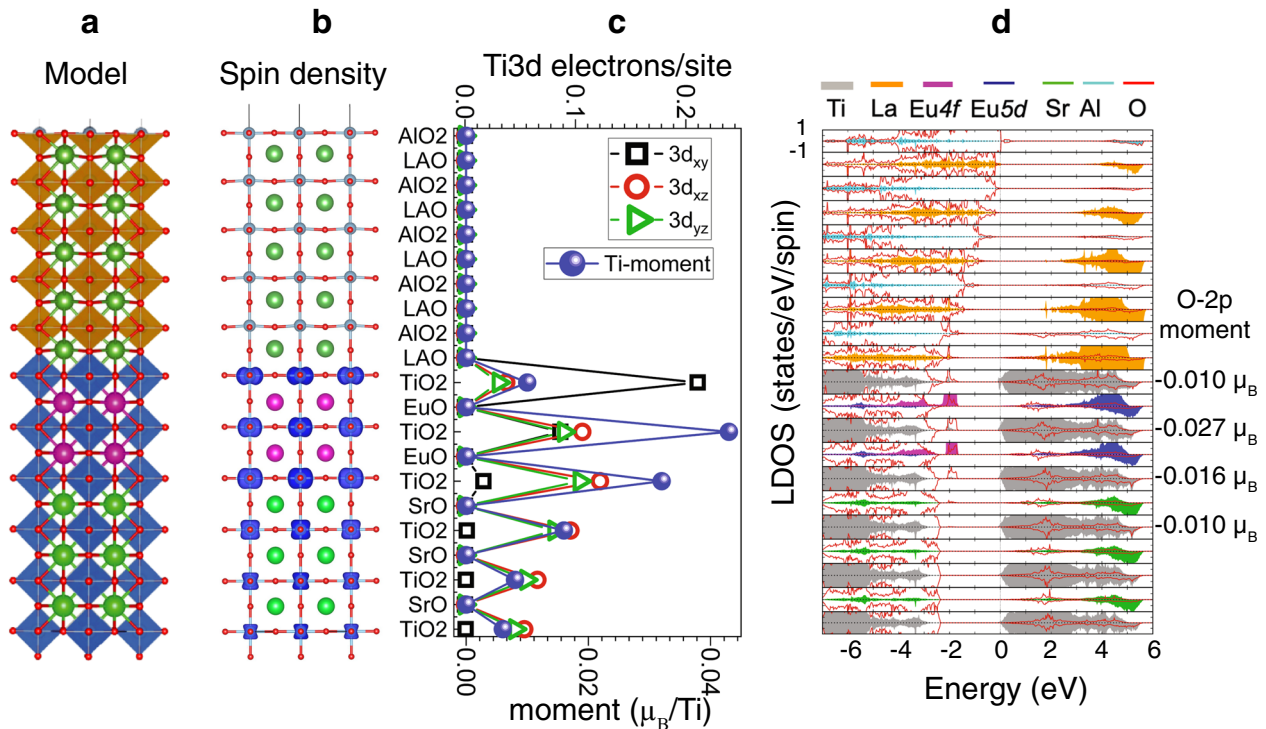


Fig. 5 DFT + U calculations. **a** Side view of the simulated $c(2 \times 2)$ LAO/ETO/STO(001) heterostructure; **b** spin density, integrated between -0.3 eV and E_F , with isovalue of $0.0004 \text{ e}/\text{\AA}^3$, showing the spatial distribution of the 2DEG and the orbital character at the Ti sites; **c** orbital and layer resolved Ti-3d occupation (upper scale; black squares, $3d_{xy}$; red circles, $3d_{xz}$; green triangles, $3d_{yz}$) and Ti-3d magnetic moment (lower scale; blue circles) obtained by integrating the density of states between -0.3 eV and E_F . **d** Layer-, spin- and element- resolved density of states. The color code for the partial LDOS contribution of different ions is indicated on top of the figure. On the right side of the figure, we also indicate the values of the calculated oxygen-2p magnetic moment in the corresponding interfacial TiO_2 layers.

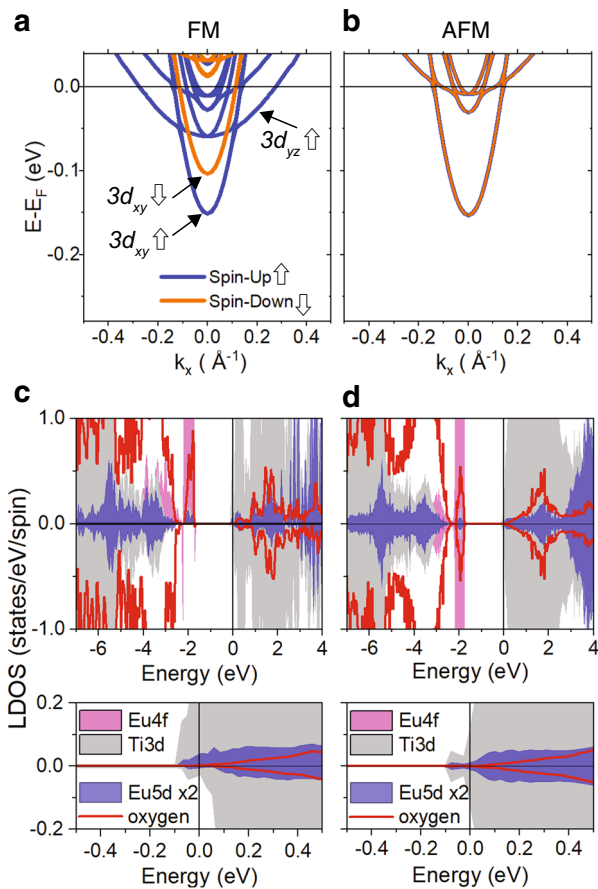


Fig. 6 Spin-resolved band structure and LDOS in the FM and AFM state from the DFT + U calculations. Spin-resolved band structure calculations of the Ti-3d bands around the Γ -point in a small energy range in the (a) FM (left panel) and (b) AFM (right panel) solutions of the model. Note that in the FM solution, the spin-up $3d_{yz}$ band shift to lower energy and crosses the Fermi level, while the $3d_{xy}$ spin-down bands shifts up, giving rise to an overall spin-polarization of the q2DEG. Element and spin-resolved density of states from the DFT + U calculations for EuTiO_3 layers (average) with (c) FM and (d) AFM coupling (same vertical scales in a, b). In the FM solution we do observe a substantial spin-polarization at -2 eV of both Eu-4f (magenta) and Eu-5d (blue) states, and an overlap between Ti-3d states (gray) and Eu-5d states near and above the Fermi level, absent in the AFM case.

2 uc of ETO and 5 uc of LAO on both sides of a symmetric TiO_2 -terminated 6.5 uc STO slab (Fig. 5a). Along the c -axis the LAO surface is separated by a vacuum region of 20 Å from its periodic images. Calculations with larger STO stacks of 10.5 uc and 14.5 uc are shown in Supplementary Fig. 7 and give qualitatively similar results. On-site effective Hubbard parameter $U = 4$ eV, 7.5 eV and 8 eV were applied on the Ti-3d, Eu-4f and La-4f states, respectively. Similar to findings for the ETO (001) surface state²⁸, the choice of U for the Eu-4f states, and partially for the Ti-3d states, is dictated by the necessity to reproduce the position of the Eu^{2+} peak in the valence band at about -2 eV. We performed calculations for both AFM (G-type) and FM arrangement of the Eu-ions. The FM solution is preferred by ~ 20 meV per simulation cell. This result is in full agreement with the experimental evidence of a FM ordering of Eu^{2+} magnetic moments shown in Figs. 1, 2 and in ref. 11.

In Fig. 5 we show also the spatial distribution of the spin density (Fig. 5b), the layer- and orbitally- resolved Ti-3d occupation and magnetic moments (Fig. 5c), as well as the layer, atom- and spin-resolved density of states across the interface (Fig. 5d). According to the DFT + U results, the q2DEG is formed as a result of the polar

discontinuity at the LAO/ETO/STO interface and surface, evidenced by the overlap between the energy positions of the O-2p band of the AlO_2 surface and of the interfacial TiO_2 3d-conduction bands in Fig. 5d, analogous to (001) LAO/STO bilayers. The spin density plotted in Fig. 5b and the layer-resolved orbital occupation in Fig. 5c show that the q2DEG is characterized by a substantial occupation of Ti-3d states within the ETO layer, which goes to zero within a few unit cells of STO.

The bands are spin-polarized, with the highest polarization within the ETO layers, which exhibit also the largest electron occupation. In particular, Fig. 5b, c shows that the $3d_{xy}$ bands are the first to be occupied at the interface and are mostly localized into the ETO film, whereas the occupied states within STO have a $3d_{xz}/3d_{yz}$ orbital character, reflecting the wider distribution of these carriers, as also observed in (001) STO³⁰. The Ti-3d magnetic moment, obtained by integrating the spin-resolved density of states in the range between -0.3 eV and E_F (i.e., the contribution from spin-polarized conduction bands) is maximum in the second ETO layer, and then goes to zero within the first three-unit cells of STO (Fig. 5c). Consequently, both ETO and the topmost STO layers host electrons which are spin-polarized. The associated Ti-3d magnetic moment is parallel to the large spin-moment of Eu^{2+} 4f states ($6.97 \mu_B$), and its order of magnitude is in overall agreement with the analysis of the XMCD data (see Supplementary Note 1). The layer resolved map in Fig. 5d shows also a finite spin-polarized electron density of Ti-3d, Eu-5d and O-2p states at the position of the Eu^{2+} peak, demonstrating a hybridization between Eu-4f, Eu-5d, O-2p and Ti-3d states, in agreement with RESPAES data. Moreover, O-2p states in the TiO_2 layers of ETO also acquire a finite magnetic moment, opposite to the Ti-3d¹ and Eu-4f⁷ magnetic moments. This can explain the two components of the XMCD spectra, one related to the $3d^0 + 3d^1L$ states, with a negative exchange interaction with the Eu^{2+} 4f states, and the other from Ti-3d¹ spin-polarized electrons, parallel to the overall magnetization direction.

In order to compare the experimentally determined band structure shown in Fig. 4 with DFT + U calculations, and to highlight the differences between the conduction bands in the FM (the ground state) and AFM solutions of the model, we show in Fig. 6 the calculated, spin-resolved, Ti-3d band structure around the Fermi level in the two cases. In the case of the AFM state, we have adopted a G-type ordering of the Eu-spin moments. The calculated band structures are qualitatively consistent with the main characteristics of the experimentally determined band properties shown in Fig. 4. In both the FM (Fig. 6a, left panel) and AFM (Fig. 6b, right panel) solutions, the lowest lying Ti-3d band crossing E_F is a dispersive parabolic band with d_{xy} orbital character, which switches at larger momentum into a much flatter band indicating an avoided crossing with the heavy bands with $3d_{xz}/3d_{yz}$ orbital character. The higher-lying bands around Γ are replicas from different layers due to the confinement of the q2DEG. In the FM solution of the model, spin-up (blue) and spin-down (orange) bands, both of the d_{xy} , and d_{xz}/d_{yz} main orbital character, are split in the whole energy range and cross the Fermi level, showing a prevalence of majority spin-polarized electrons in the system, in full agreement with all the experimental evidences of FM correlations in the q2DEG. In the AFM case the spin-degenerate $3d_{xy}$ bands arrange in the same energy region as the spin-up band of the FM phase, while $3d_{xz}/3d_{yz}$ bands are lifted above the Fermi level. Thus, the conduction band minimum, associated with the lowest $3d_{xy}$ band is the same in both AFM and FM phases, but all the other bands are shifted in the FM solution. The DFT + U calculations in particular show a down-shift of the spin-up $3d_{xz}/3d_{yz}$ bands and more importantly a filling of these bands taking place only in the FM ground state. Thus, ferromagnetism appears simultaneously with the orbital selective filling of $3d_{xz}/3d_{yz}$ electrons at the Fermi level, confirming their

crucial role in establishing FM correlations in the q2DEG as earlier suggested in ref. ¹¹.

DISCUSSION

The experimental and theoretical results on LAO/ETO/STO (001) heterostructure show an interaction between Eu^{2+} -4f and Ti-3d states. This is rather surprising considering the large value of the Hubbard parameter on the 4f orbitals, and their strong electron localization, rendering them not far from a configuration with electrons frozen in the core.

In bulk EuTiO_3 , the establishment of a FM ground state, instead of an AFM one, is believed to be due to a delicate balance between the different exchange interactions among Eu^{2+} magnetic moments in the system: i) Direct FM exchange between Eu^{2+} , which is very weak due to the almost null overlap between Eu-4f orbitals; ii) an AFM super-exchange interaction mediated by O-2p states; iii) an AFM super-exchange interaction mediated by Ti-3d states; iv) a carriers mediated Ruderman-Kittel-Kasuya-Yoshida (RKKY)-like indirect FM-exchange, proposed for Layered FM ETO films¹⁷, due to an overlap between (filled) t_{2g} Ti-3d and Eu 4f-orbitals; and v) an indirect exchange interaction via Eu-5d t_{2g} states, which play an important role in Eu-chalcogenides (e.g., EuO). It has been proposed that the filling of the Ti-3d bands reverts the indirect exchange via the Eu-5d t_{2g} states from AFM to FM through the coupling between t_{2g} Eu-5d and Ti-3d electrons^{43,44}. Our experimental XMCD data confirm that the super-exchange between Eu^{2+} magnetic moments through O-2p and Ti-3d states is negative, thus the only two mechanisms which could effectively give rise to ferromagnetism are FM-couplings mediated by itinerant carriers (without any role of Eu-5d states) or mediated by Eu-5d hybridized with Ti-3d states⁴⁴.

In order to verify if the latter can effectively play a role in our heterostructures, in Fig. 6c we show the spin-resolved LDOS of the ETO layers in the FM ground state. The calculations are compared to the LDOS in the AFM configuration (Fig. 6d). We find that Eu-5d states, while in general characterized by a much weaker spectral weight than the O-2p and Ti-3d contributions, have a strong overlap with Ti-3d t_{2g} bands in the FM ground state close and above the Fermi level. Furthermore, there is also a substantial overlap with the Eu-4f state around -2 eV, where these states also show a clear spin-polarization. On the other hand, in the AFM solution the Eu-5d states are at higher energy, have a lower spectral weight compared to the FM-case, and their overlap with Ti-3d states is substantially reduced. These results suggest that the FM-ordering of Eu^{2+} is mostly due to a FM interaction mediated by Eu-5d/Ti-3d hybridized states as suggested earlier⁴⁴, although it is not possible to fully exclude a role of a carrier-mediated RKKY-FM interaction¹⁷.

Interestingly the calculations also demonstrate that the filling of Ti-3d_{xz}/3d_{yz} bands and FM-order appear concomitantly, as shown in Fig. 6a. Therefore, Ti-3d_{xz}/3d_{yz} electrons play an essential role in the establishing a FM-coupling among the Eu^{2+} magnetic moments in the confined heterostructure, while the 3d_{xy} electrons seems less effective in mediating a dominant FM interaction in this system.

To summarize, in this work we combined different experimental methods and theoretical calculations to analyze and clarify the origin and properties of the spin-polarized q2DEG at the LAO/ETO/STO oxide interface. The DFT + *U* calculations show that a FM and spin-polarized q2DEG is formed at the defect-free interfaces in the (001) LAO/ETO/STO heterostructure. At the same time, theory explains some crucial properties of this q2DEG revealed by x-ray spectroscopy and electrical transport results. In particular, it is shown that the filling of 3d_{xz}/3d_{yz} bands, inferred from the experimental results, is simultaneous to the transition to a FM state, thus explaining why the q2DEG is spin-polarized only above the Lifshitz transition. Moreover, spin-polarized 3d_{xz}/3d_{yz} electrons

created at the LAO/ETO interface leak also into the first layers of STO, explaining the contribution from STO to the Ti-3d magnetic moment found in previous investigations¹¹.

Our results show that the LAO/ETO/STO system provides a platform for the study of emerging quantum phenomena where superconductivity, magnetism and spin-orbit coupling are fully entangled, and is a clear example on how functional properties can be created in oxide 2D-systems by atomic interface engineering.

More generally, the combination of electrical transport and spectroscopy measurements with band structure calculations reported in this work is a powerful tool to obtain a deeper understanding of complex heterostructures characterized by unexpected functional properties. Such a combined approach is becoming essential to gain detailed understanding of heterostructures showing exceptional properties.

METHODS

Samples preparation

LAO(*n*)/ETO(2)/STO(001) heterostructures were fabricated by PLD assisted by Reflection High Energy Electron Diffraction (RHEED) from sintered $\text{Eu}_2\text{Ti}_2\text{O}_7$ and crystalline LAO targets onto TiO_2 -terminated (001) STO substrates. The samples were deposited at a temperature of 700 °C in a background O_2 pressure of 8×10^{-5} mbar and cooled down in the same conditions to room temperature with a rate of 5 °C/min. We used an excimer laser (Lambda Physics, 248 nm wavelength) and 1.3 J/cm² fluence, 1 Hz of repetition, resulting in a rate of 0.05 uc/pulse (20 pulses for each unit cells). A q2DEG is formed when $n > 4$ uc.

XAS, XLD and XMCD spectroscopy measurements

We have used polarization dependent x-ray absorption spectroscopy (XAS) across the Eu $M_{4,5}$ and the Ti- $L_{2,3}$ edge to probe directly the magnetic and orbital properties of Eu and Ti at the interface. The experiments were performed at the beamline X-Treme of the Swiss Light Source²⁴. XAS performed with circularly or linearly polarized photons can detect the magnetic moments and the 3d-orbital energy splitting, respectively. The two techniques, usually known as x-ray magnetic circular dichroism (XMCD) and x-ray linear dichroism (XLD) are so sensitive that they can be used on single interfaces. The Eu $M_{4,5}$ edge and the Ti $L_{2,3}$ XMCD spectra were obtained as difference between the average of 8 and 16 (respectively) XAS spectra acquired with magnetic field parallel and antiparallel to the photon-helicity vector orientations. The 16 and 32 XAS data needed for each XMCD were collected in a sequence alternating reversal of field and polarization at each spectrum. This procedure ensures the best cancellation of spurious effects. The magnetic field dependent magnetization loops, as those shown in Fig. 1, were obtained by measuring, at each field, the difference between the TEY intensity at the M_5 -Eu edge peak, normalized by the intensity below the absorption edge, obtained with two different helicities (combination with polarization and field direction).

Squid magnetometry measurements

SQUID data were collected by using a Quantum Design MPMS3 magnetometer at the Université de Strasbourg, IPCMS. Magnetization measurements as a function of magnetic field were acquired on both LAO/ETO/STO heterostructure and bare STO substrates that suffered the same heating process mimicking the LAO/ETO growth to exclude the presence of ferromagnetic impurities stemming from the substrate itself. Data were corrected for the diamagnetism of the substrate substrating the linear contribution acquired at high magnetic fields.

RESPES measurements

RESPES Measurements were carried out at a pressure of 5×10^{-10} mbar and at base temperature of ≈ 12 K (above the FM T_c) on LAO(5)/ETO(2uc)/STO samples. This technique, employing soft-energy x-rays resonant with the absorption of the relevant ions in the system, enables access to buried systems, and it is, therefore, suitable for the investigation of the q2DEG at the LAO/ETO/STO interface. To reduce any influence of contaminants and to preserve as much as possible the surface of the ex-situ grown samples,

they were transferred, just after the deposition, into a sample-carrier vessel filled by inert Ar-gas. However, an exposure (limited in time) to ambient atmosphere was unavoidable for the sample mounting into the experimental station. During the measurements we moved the beam position around the region investigated in order to avoid variations of the surface and interfacial oxygen by photon irradiation, to which LAO/STO samples of certain preparation protocols have demonstrated some sensitivity at low temperature²⁷. As a matter of fact, by raster scanning the beam on the sample, we did not detect any buildup of the Ti^{3+} spectral weight, neither in the core level x-ray photoemission (XPS) and XAS spectra, nor in the valence band (VB).

DFT + U calculations

DFT + U calculations were performed with the Vienna ab initio simulation package (VASP) (39, 40)^{36,37} with the projector augmented wave (PAW) basis^{38,39}. The generalized gradient approximation of Perdew, Burke and Ernzerhof⁴⁰ and an on-site effective Hubbard parameter⁴¹, $U = 4$ eV, 7.5 eV and 8 eV were applied on the Ti-3d, Eu-4f and La-4f states, respectively. Analogous to the ETO (001) surface state²⁸, the choice of U for the Eu-4f states, and partially for the Ti-3d states, is dictated by the need to reproduce the position of the experimental Eu^{2+} peak in the valence band at ~ 2 eV. In general, lower values of U for Eu-4f only shift the position of the Eu-4f band to energies closer to the Fermi level. The results shown here for $U = 4$ eV for the Ti-3d states give the best agreement with the experimental data, and in particular concerning the position of Eu-4f band. Calculations with U ranging from 1 eV to 4.5 eV show that the main conclusions are not dependent on the choice of U for Ti-3d states (see Supplementary Fig. 6).

The simulated supercell consists of a symmetric TiO_2 -terminated 6.5 uc thick STO part followed by 2 uc ETO and 5 uc LAO on each side. The LAO surface is separated by 20 Å of vacuum from its periodic images to avoid interaction through the vacuum. The resulting structure contains 206 ions. Simulations were also performed with a thicker STO part, containing four and eight additional STO layers (a total of 246 and 286 ions), respectively, showing qualitatively similar results, as shown in Supplementary Note 1.

We used a $8 \times 8 \times 1$ Monkhorst-Pack k -point grid⁴² and a cut-off energy of 400 eV for the basis set. The ionic positions were fully relaxed until the forces were less than 0.001 eV/Å.

DATA AVAILABILITY

All data needed to evaluate the conclusions in the paper are present in the paper and/or in the Supplementary Information. The datasets generated and/or analyzed during the current study are available from the corresponding author on reasonable request.

CODE AVAILABILITY

The code that supports the findings of this study is available from the corresponding author upon reasonable request.

Received: 29 September 2021; Accepted: 15 March 2022;

Published online: 08 April 2022

REFERENCES

- Ohtomo, A. & Hwang, H. Y. A high-mobility electron gas at the $LaAlO_3/SrTiO_3$ heterointerface. *Nature* **427**, 423–426 (2004).
- Thiel, A. et al. Tunable quasi-two-dimensional electron gases in oxide heterostructures. *Science* **313**, 1942–1946 (2006).
- Caviglia, A. D. et al. Tunable Rashba spin-orbit interaction at oxide interfaces. *Phys. Rev. Lett.* **104**, 126803 (2010).
- Stornaiuolo, D. et al. Weak localization and spin-orbit interaction in side-gate field effect devices at the $LaAlO_3/SrTiO_3$ interface. *Phys. Rev. B* **90**, 235426 (2014).
- Caviglia, A. D. et al. Electric field control of the $LaAlO_3/SrTiO_3$ interface ground state. *Nature* **456**, 624–627 (2008).
- Richter, C. et al. Interface superconductor with gap behaviour like a high-temperature superconductor. *Nature* **502**, 528–531 (2013).
- Stornaiuolo, D. et al. Signatures of unconventional superconductivity in the $LaAlO_3/SrTiO_3$ two-dimensional system. *Phys. Rev. B* **95**, 140502(R) (2017).

- Brinkman, A. et al. Magnetic effects at the interface between non-magnetic oxides. *Nat. Mater.* **6**, 493–496 (2007).
- Lesne, E. et al. Highly efficient and tunable spin-to-charge conversion through Rashba coupling at oxide interfaces. *Nat. Mater.* **15**, 1261–1266 (2016).
- De Luca, G. M. et al. Transport properties of a quasi-two-dimensional electron system formed in $LaAlO_3/EuTiO_3/SrTiO_3$ heterostructures. *Phys. Rev. B* **89**, 224413 (2014).
- Stornaiuolo, D. et al. Tunable spin polarization and superconductivity in engineered oxide interfaces. *Nat. Mater.* **15**, 278–284 (2016).
- Zhang, H. R. et al. Magnetic two-dimensional electron gas at the manganite-buffered $LaAlO_3/SrTiO_3$ interface. *Phys. Rev. B* **96**, 195167 (2017).
- Moetakef, P. et al. Electrostatic carrier doping of $GdTiO_3/SrTiO_3$ interfaces. *Appl. Phys. Lett.* **98**, 112110 (2011).
- Gunkel, F. et al. Defect-control of conventional and anomalous electron transport at complex oxide interfaces. *Phys. Rev. X* **6**, 031035 (2016).
- Kormondy, K. J. et al. Large positive linear magnetoresistance in the two-dimensional t_{2g} electron gas at the $EuO/SrTiO_3$ interface. *Sci. Rep.* **8**, 7721 (2018).
- Gan, Y. et al. Diluted oxide interfaces with tunable ground states. *Adv. Mater.* **31**, 1805970 (2019).
- Katsufuji, T. & Tokura, Y. Transport and magnetic properties of a ferromagnetic metal: $Eu_{1-x}R_xTiO_3$. *Phys. Rev. B* **60**, R15021 (1999).
- Takahashi, K. S., Onoda, M., Kawasaki, M., Nagaosa, N. & Tokura, Y. Control of the anomalous hall effect by doping in $Eu_{1-x}La_xTiO_3$ thin films. *Phys. Rev. Lett.* **103**, 057204 (2009).
- Takahashi, K. S. et al. Anomalous Hall effect derived from multiple Weyl nodes in high-mobility $EuTiO_3$ films. *Sci. Adv.* **4**, eaar7880 (2018).
- Ahadi, K. et al. Carrier density control of magnetism and Berry phases in doped $EuTiO_3$. *APL Mater.* **6**, 056105 (2018).
- Lee, J. H. et al. A strong ferroelectric ferromagnet created by means of spin-lattice coupling. *Nature* **466**, 954–958 (2010).
- Piamonteze, C. et al. X-Treme beamline at SLS: X-ray magnetic circular and linear dichroism at high field and low temperature. *J. Synchrotron Rad.* **19**, 661–674 (2012).
- Stavitski, E. & de Groot, F. M. F. The CTM4XAS program for EELS and XAS spectral shape analysis of transition metal L edges. *Micron* **41**, 687–694 (2010).
- Piamonteze, C., Miedema, P. & de Groot, F. M. F. Accuracy of the spin sum rule in XMCD for the transition-metal L edges from manganese to copper. *Phys. Rev. B* **81**, 184410 (2009).
- Nagaosa, N., Sinova, J., Onoda, S., MacDonald, A. H. & Ong, N. P. Anomalous Hall effect. *Rev. Mod. Phys.* **82**, 1539–1592 (2010).
- Strocov, V. N. et al. High-resolution soft X-ray beamline ADDRESS at the Swiss Light Source for resonant inelastic X-ray scattering and angle-resolved photoelectron spectroscopies. *J. Synchrotron Rad.* **17**, 631–643 (2010).
- Chikina, A. et al. Orbital ordering of the mobile and localized electrons at oxygen-deficient $LaAlO_3/SrTiO_3$ interfaces. *ACS Nano* **12**, 7927 (2018).
- Di Capua, R. et al. Two-dimensional electron gas at the (001) surface of ferromagnetic $EuTiO_3$. *Phys. Rev. Res.* **3**, L042038 (2021).
- Haverkort, M. et al. Determination of the orbital moment and crystal-field splitting in $LaTiO_3$. *Phys. Rev. Lett.* **94**, 056401 (2005).
- Plumb, N. C. et al. Mixed dimensionality of confined conducting electrons in the surface region of $SrTiO_3$. *Phys. Rev. Lett.* **113**, 086801 (2014).
- Wang, Z. et al. Tailoring the nature and strength of electron–phonon interactions in the $SrTiO_3(001)$ 2D electron liquid. *Nat. Mater.* **15**, 835–840 (2016).
- Berner, G. et al. Direct k-space mapping of the electronic structure in an oxide-oxide interface. *Phys. Rev. Lett.* **110**, 247601 (2013).
- Cancellieri, C. et al. Doping-dependent band structure of $LaAlO_3/SrTiO_3$ interfaces by soft x-ray polarization-controlled resonant angle-resolved photoemission. *Phys. Rev. B* **89**, 121412(R) (2014).
- Cancellieri, C. et al. Polaronic metal state at the $LaAlO_3/SrTiO_3$ interface. *Nat. Commun.* **7**, 10386 (2016).
- Zhang, P. et al. A precise method for visualizing dispersive features in image plots. *Rev. Sci. Instrum.* **82**, 043712 (2011).
- Kresse, G. & Hafner, J. Ab initio molecular dynamics for liquid metals. *Phys. Rev. B* **47**, 558(R) (1993).
- Kresse, G. & Furthmüller, J. Efficiency of ab-initio total energy calculations for metals and semiconductors using a plane-wave basis set. *Comput. Mater. Sci.* **6**, 15–50 (1996).
- Blöchl, P. E. Projector augmented-wave method. *Phys. Rev. B* **50**, 17953 (1994).
- Kresse, G. & Joubert, D. From ultrasoft pseudopotentials to the projector augmented-wave method. *Phys. Rev. B* **59**, 1758 (1999).
- Perdew, J. P. et al. Restoring the density-gradient expansion for exchange in solids and surfaces. *Phys. Rev. Lett.* **100**, 136406 (2008).
- Dudarev, S. L. et al. Electron-energy-loss spectra and the structural stability of nickel oxide: an LSDA+ U study. *Phys. Rev. B* **57**, 1505 (1998).

42. Monkhorst, H. J. & Pack, J. D. Special points for Brillouin-zone integrations. *Phys. Rev. B* **13**, 5188 (1976).
43. Akamatsu, H. et al. Antiferromagnetic superexchange via 3d states of titanium in EuTiO_3 as seen from hybrid Hartree-Fock density functional calculations. *Phys. Rev. B* **83**, 214421 (2011).
44. Gui, Z. & Janotti, A. Carrier-density-induced ferromagnetism in EuTiO_3 bulk and heterostructures. *Phys. Rev. Lett.* **123**, 127201 (2019).

ACKNOWLEDGEMENTS

The Authors acknowledge funding from ERA-NET QUANTERA European Union's Horizon H2020 project QUANTOX under Grant Agreement No. 731473, Ministero dell'Istruzione, dell'Università e della Ricerca (MIUR) for the PRIN project TOP-SPIN (Grant No. PRIN 201775L7HC) and for the PRIN 2010-11 project (Grant No. PRIN 2010-11-OXIDE), the EU COST program CA16218 (Nanocohybri), the German Research Foundation (DFG) within CRC/TRR80 (project number 107745057, subproject C3), CRC1242 (project number 278162697, subproject C02), and Computation time at the Leibniz Rechenzentrum Garching, project pr87ro and supercomputer magnitUDE (DFG grants INST 20876/209-1 FUGG, INST 20876/243-1 FUGG).

AUTHOR CONTRIBUTIONS

Conceptualization: R.D.C., D.S., G.G., M.S. Methodology: Sample preparation: A.S., E.D.G., F.M.G., Y.C., M.S. Transport measurements and Analysis: B.J., D.S., Y.C., M.D.A. RESPES Experiment and Analysis: R.D.C., V.N.S., M.S., M.R., E.G., E.D.G., F.M.G. ARPES Experiment: M.R., G.M.D.L., R.D.C., B.G., N.P., M.S. XMCD Experiment and Analysis: C.P., M.S., G.G., G.M.D.L., D.P. SQUID Experiment: D.P. DFT+U Calculations: M.V., R.P. Supervision: M.S., R.P., D.S. Writing: M.S., D.S., R.D.C., R.P. Writing-review & editing: all the Authors participated to the editing of the paper.

COMPETING INTERESTS

The authors declare no competing interests.

ADDITIONAL INFORMATION

Supplementary information The online version contains supplementary material available at <https://doi.org/10.1038/s41535-022-00448-4>.

Correspondence and requests for materials should be addressed to M. Salluzzo.

Reprints and permission information is available at <http://www.nature.com/reprints>

Publisher's note Springer Nature remains neutral with regard to jurisdictional claims in published maps and institutional affiliations.



Open Access This article is licensed under a Creative Commons Attribution 4.0 International License, which permits use, sharing, adaptation, distribution and reproduction in any medium or format, as long as you give appropriate credit to the original author(s) and the source, provide a link to the Creative Commons license, and indicate if changes were made. The images or other third party material in this article are included in the article's Creative Commons license, unless indicated otherwise in a credit line to the material. If material is not included in the article's Creative Commons license and your intended use is not permitted by statutory regulation or exceeds the permitted use, you will need to obtain permission directly from the copyright holder. To view a copy of this license, visit <http://creativecommons.org/licenses/by/4.0/>.

© The Author(s) 2022